Check for updates

Identification of weak molecular absorption in single-wavelength s-SNOM images

IRIS NIEHUES,[1,*] LARS MESTER,[2] EDOARDO VICENTINI,[1]
DANIEL WIGGER,[3] MARTIN SCHNELL,[1,4]
AND RAINER HILLENBRAND[1,4,5,6]

[1]*CIC nanoGUNE BRTA, 20018 Donostia-San Sebastián, Basque Country, Spain*
[2]*attocube systems AG, Eglfinger Weg 2, 85540, Munich-Haar, Germany*
[3]*School of Physics, Trinity College Dublin, Dublin 2, Ireland*
[4]*IKERBASQUE, Basque Foundation for Science, 48013 Bilbao, Basque Country, Spain*
[5]*Department of Electricity and Electronics, UPV/EHU, 20018 Donostia-San Sebastián, Spain*
[6]*r.hillenbrand@nanogune.eu*
*i.niehues@nanogune.eu

Abstract: Scattering-type scanning near-field optical microscopy (s-SNOM) allows for nanoscale optical mapping of manifold material properties. It is based on interferometric recording of the light scattered at a scanning probe tip. For dielectric samples such as biological materials or polymers, the near-field amplitude and phase signals of the scattered field reveal the local reflectivity and absorption, respectively. Importantly, absorption in s-SNOM imaging corresponds to a positive phase contrast relative to a non-absorbing reference sample. Here, we describe that in certain conditions (weakly or non- absorbing material placed on a highly reflective substrate), a slight negative phase contrast may be observed, which can hinder the recognition of materials exhibiting a weak infrared absorption. We first document this effect and explore its origin using representative test samples. We then demonstrate straightforward simple correction methods that remove the negative phase contrast and that allow for the identification of weak absorption contrasts.

1. Introduction

Scattering-type scanning near-field optical microscopy (s-SNOM) is a technique that allows for optical imaging of a large variety of samples with a spatial resolution of about 25 nm [1,2]. It is based on elastic light scattering from a standard metalized atomic force microscope (AFM) tip, which is illuminated with monochromatic laser light. Acting as an optical antenna, the tip converts the illuminating field into a strongly concentrated near field at the tip apex (nanofocus), which interacts with the sample surface. Interferometric recording of the scattered field as a function of sample position yields near-field amplitude and phase images (simultaneously to the AFM topography image) [3], which encode information about the local dielectric function of the sample. By replacing the monochromatic laser with a broadband laser light source and recording the tip-scattered light with an asymmetric Fourier-transform (FT) spectrometer one can record complex-valued (i.e. amplitude and phase resolved) infrared (IR) spectra with a nanoscale spatial resolution (nano-FTIR spectroscopy) [4–8]. In both cases the tip oscillates at a frequency Ω (typically close to the mechanical resonance frequency of the AFM cantilever; tapping mode AFM) and demodulation of the detector signal at the n-th harmonic $n\Omega$ is applied to supress unavoidable background signals, yielding background-free amplitude and phase signals, s_n and φ_n, respectively [3]. For dielectric samples the s_n and φ_n signals essentially reveal the local reflectivity and absorption of the material, respectively, allowing for nanoscale material

identification based on standard infrared references [9–11]. Importantly, when a dielectric material (such as a biological or a polymeric material) absorbs the incident light, the near-field phase contrast between the material (mat) and the non-absorbing highly reflecting substrate (ref) is positive, $\varphi_n = \varphi_{n,\text{mat}} - \varphi_{n,\text{ref}} > 0$ [4–10,12–25]. For non-absorbing materials, the phase contrast relative to the non-absorbing reflective substrate should vanish, $\varphi_n = 0$. However, the phase of non-absorbing or only weakly absorbing materials can unexpectly assume negative values relative to a non-absorbing reference, which has been observed [10,20,21,23,24,26,27] but not discussed and explained so far. Such negative phase contrasts may challenge the interpretation of material properties, particularly when only little is known about the sample and its composition. Here, we document this puzzling effect, which we refer to as negative phase contrast (NPC). We find that the NPC appears for thin films of organic or inorganic materials on highly reflecting substrates, and that it depends on the film thickness. First, we perform systematic studies to clarify the origin of the NPC (Secs. 2,3). More importantly, we develop simple methods for correcting the NPC in s-SNOM imaging (Sec. 4).

2.   Documentation of the negative phase contrast

We demonstrate the NPC with a typical sample often studied in s-SNOM, which comprises layers of polystyrene (PS) and polymethyl-methacrylate (PMMA) on a silicon (Si) substrate. The experiments were performed with a commercial s-SNOM/nano-FTIR instrument (*neaSNOM from attocube systems AG*, comprising a quantum cascade laser for imaging and broadband laser source for spectroscopy) and standard PtIr-coated AFM tips (*Arrow NCPt* from *Nanoworld AG*) with an apex radius of about 25 nm. Figure 1(a) shows the AFM topography image of the PMMA/PS sample. Line profiles taken along the horizontal blue and red dashed lines across the PMMA and PS regions (bottom) show that the PMMA and PS layers are 60 nm and around 40-55 nm thick, respectively. For s-SNOM imaging in Fig. 1(b) we chose a wavenumber where PMMA is non-absorbing ($1680\,\text{cm}^{-1}$), another one where PMMA is weakly absorbing ($1710\,\text{cm}^{-1}$), and a third one where PMMA is strongly absorbing ($1735\,\text{cm}^{-1}$). Note that PS is non-absorbing at all chosen wavenumbers. The corresponding phase images φ_3 are shown in the top panel of Fig. 1(b) (the corresponding amplitude images are shown in Supplement 1, Fig. S1). All images are normalized (i.e. referenced) to the phase value of the Si reference substrate ($\varphi_3 = \varphi_{3,\text{PMMA}} - \varphi_{3,\text{Si}}$). Note that a positive phase contrast relative to the Si substrate is displayed by redish colors and negative phase contrast by blueish colors. As expected, the strong absorption of PMMA at $1735\,\text{cm}^{-1}$ (right panel, associated with the C=O stretching mode [28,29]) yields a strong positive phase contrast of about $\varphi_3 = 55°$ (see also line profiles in Fig. 1(b) bottom). For PS we expect a vanishing phase contrast at $1735\,\text{cm}^{-1}$, as it is not absorbing at this wavenumber. However, a negative phase contrast of about $\varphi_3 = -5°$ is observed for the PS layer, which can be consistently reproduced at other wavenumbers, where PS is non-absorbing ($1680\,\text{cm}^{-1}$ and $1710\,\text{cm}^{-1}$; see also Supplement 1, Figs. S2 and S3 for more wavenumbers). The nearly same negative phase contrast can also be seen for PMMA at $1680\,\text{cm}^{-1}$ (left panel), where PMMA is non-absorbing. Importantly, the PMMA phase contrast is also slightly negative at $1710\,\text{cm}^{-1}$ (middle panel) although the PMMA absorption is not negligible at this wavenumber (see nano-FTIR spectrum of Fig. 1(c) and discussion below).

To explore how the NPC affects near-field phase spectra, we took a series of s-SNOM amplitude and phase images between $1680\,\text{cm}^{-1}$ and $1800\,\text{cm}^{-1}$ (all of them shown in Supplement 1, Fig. S2) and extracted phase values to construct a near-field phase spectrum of the PMMA layer (blue dots in Fig. 1(c)). Each dot is extracted from one phase image – measured with the same parameters, the same tip and on the same sample position as the ones in Fig. 1(b) – by taking the mean value of the phase in the PMMA sample region indicated by the blue rectangle in the topography image (Fig. 1(a)). We find negative phase values on the PMMA layer for wavenumbers where the PMMA is non- or weakly absorbing (i.e. below $1710\,\text{cm}^{-1}$ and above
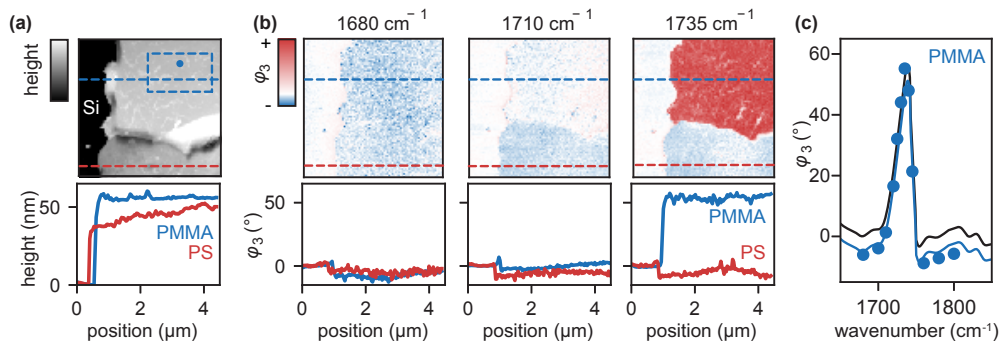
Fig. 1. Negative phase contrast (NPC) on PMMA and PS layers on a Si substrate. Images where taken with a tip oscillation amplitude of around 65 nm. (a) Top: AFM topography image showing Si substrate, PS, and PMMA. Bottom: line profiles extracted along the dashed lines in the AFM image. (b) Top: s-SNOM phase images φ_3 recorded at $1680\,cm^{-1}$, $1710\,cm^{-1}$, and $1735\,cm^{-1}$. Bottom: Line profiles extracted from the phase images along the dashed lines. c) Near-field phase spectrum of the PMMA layer. Blue dots: Phase values extracted from the PMMA region marked with the rectangle in (a) of the s-SNOM images shown in (b) (see also Supplement 1, Fig. S2). Blue curve: nano-FTIR phase spectrum φ_3 of PMMA taken at the position marked by the blue dot in (a). Black curve: baseline-corrected nano-FTIR phase spectrum φ_3^c of PMMA. The nano-FTIR spectrum was taken with an integration time of 30 ms/pixel and a spectral resolution of $6.0\,cm^{-1}$. The tip oscillation amplitude was set aorund 45 nm. A zero filling factor of 16 was applied.

$1760\,cm^{-1}$), yielding a negative spectral baseline. For comparison, we also recorded a nano-FTIR amplitude and phase spectrum of the PMMA layer at the position indicated with the blue dot in the topography image (Fig. 1(a)). The blue curve in Fig. 1(c) shows the nano-FTIR phase spectrum normalized to that of the Si substrate (see Supplement 1, Fig. S4), confirming both the PMMA peak and the negative baseline. We note that the nano-FTIR spectra on PMMA and reference (Si) were measured with a minimal time delay of about 30 s. We could thus avoid a baseline correction of the normalized nano-FTIR spectrum, which is often applied in nano-FTIR spectroscopy to remove baseline tilts that are caused by drifts of the white light position (WLP) of the FT spectrometer between sample and reference measurements [30]. The baseline correction automatically eliminates the NPC, which thus is often not recognized (and not disturbing) in nano-FTIR spectroscopy (black curve in Fig. 1(c), see methods and Supplement 1, Fig. S4). In single-wavelength s-SNOM imaging, however, a NPC can prevent recognition of weakly absorbing materials. For example, PMMA does not exhibit a clear positive contrast ($\varphi_3 \approx 0$) in the phase image at $1710\,cm^{-1}$ (Fig. 1(b) middle panel), although it already weakly absorbs when compared to the negative spectral phase baseline (Fig. 1(c)). Molecular vibrations exhibiting significantly weaker absorption than the very strong C=O bond of PMMA might thus not be recognized by single s-SNOM imaging.

3. Exploring the origin of negative phase contrast

To explore the origin of the NPC, we prepared a sample comprising differently thick layers of a non-absorbing material on top of a gold (Au) layer and performed various experiments as described in the following. We have chosen hBN as the material because of the easy layer fabrication by dry exfoliation and the absence of absorption around $1000\,cm^{-1}$, as well as to demonstrate that the NPC is not specific for organic materials such as PMMA.

In a first s-SNOM experiment (illustrated in Fig. 2(a), top), we imaged an hBN layer with a thickness of 90 nm (measured from the topography image in Fig. 2(a), bottom) at $1000\,cm^{-1}$. As

before with the non-absorbing PS and PMMA layers, we observe a significant negative contrast in the phase image and line profile, amounting to $\varphi_3 = -18°$ (Fig. 2(b) top and bottom, respectively, corresponding amplitude images are shown in Supplement 1, Fig. S5). After covering the entire sample with a 50 nm thick Au layer (illustrated in Fig. 2(d), top), the NPC vanishes (Fig. 2(e)), which lets us exclude that topography (i.e. the change of purely the sample height) is the origin of the NPC. The positive phase contrast observed near the Au-covered hBN edge we attribute to indirect tip illumination [23] due to far-field reflection of the incident beam at the Au-coated Au substrate (indicated by the left E_{inc}^r arrow in Fig. 2(d)).
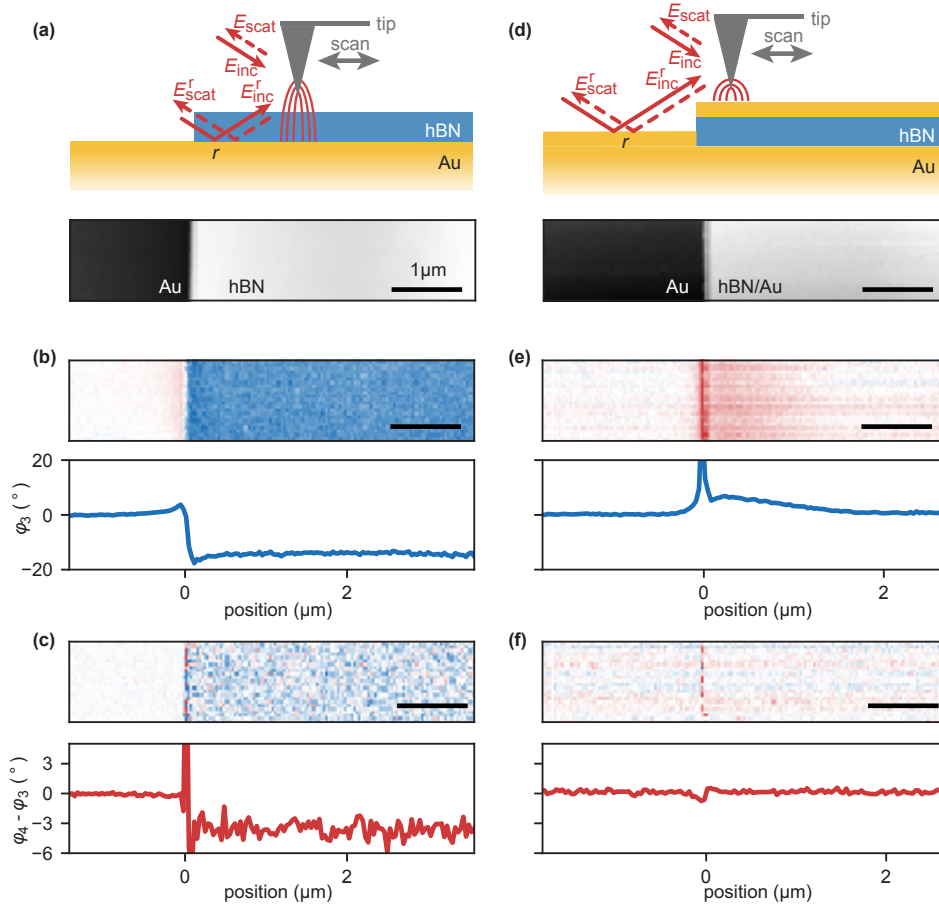

Fig. 2. s-SNOM phase images φ_3 and corresponding line profiles. Left column: hBN on Au substrate; Right column: Same sample but covered with an additional 50 nm thick Au layer. Images where taken with a tip oscillation amplitude of around 65 nm. (a,d) Top: Schematic of sample and experiment. Bottom: AFM topography image. The thickness of the hBN flake is 90 nm. (b,e) Top: s-SNOM phase image φ_3 recorded at $1000\,cm^{-1}$; Bottom: extracted line profile (averaged over depicted area). (c,f) Top: Calculated phase difference images $\varphi_4 - \varphi_3$; Bottom: extracted line profiles (φ_4 is shown in Supplement 1, Fig. S6).

We next explore whether the NPC is caused by the indirect tip illumination via reflection at the sample surface, which can potentially disturb local near-field contrasts [23]. As illustrated by the red arrows in Fig. 2(a), the tip is not only illuminated by the incident field E_{inc} directly but also indirectly by the field reflected at the hBN/Au surface , E_{inc}^r, owing to the diffraction-limited size of the laser focus. The tip-scattered field can thus be described by $E_{scat} \propto (1 + cr)^2 E_{inc}$, where

c is a constant factor and $r = |r|e^{i\Theta}$ is the complex-valued multilayer reflection coefficient of the hBN/Au sample with Θ being the reflection phase [23,31]. As in s-SNOM the tip is fixed and the sample is moved vertically to compensate for topography changes when the sample is scanned laterally, the phase of the scattered field increases with increasing hBN thickness (as the reflection phase Θ increases), yielding a positive phase contrast (e.g. seen in Fig. 2(e) near the Au-coated hBN edge) that is actually contrary to the observed NPC. We thus can exclude that indirect tip illumination is the cause for the observed negative phase contrast. For an experimental verification, we eliminate the indirect illumination. As demonstrated in Ref. [23], this can be achieved by plotting the difference of phase data obtained at the forth and third signal demodulation order, $\varphi_4 - \varphi_3$. The corresponding phase image and line profile in Fig. 2(c) show that the negative phase contrast between the hBN layer and Au surface is maintained, revealing that the NPC is a near-field contrast (see Supplement 1, Fig. S6 for φ_4). We note that the fully Au-covered sample (Fig. 2(f)) does not show any phase contrast between the left (lower) and right (upper) surface, which is an expected result as both surfaces are homogeneously coated by Au. We also find that the positive phase contrast near the Au-coated hBN edge in Fig. 2(e) is eliminated, verifying that it is caused by indirect tip illumination via far-field reflection at the Au-covered Au substrate.

To gain further insights, we retracted the oscillating tip (as illustrated in Fig. 3(a); tapping amplitude of 57 nm) from the sample surface and measured the near-field amplitude s_3 and phase φ_3 signals above the Au and hBN surface as a function of tip-sample distance h (also called retraction curve; illumination with $1000\,\text{cm}^{-1}$; same sample as in Figs. 2(a–e)). Figures 3(b–c) display the optical signals as commonly shown in literature [32], with $h = 0$ being defined as the first contact between tip apex and surface (see Fig. 3(a)). Further, the amplitude and phase signals of Au (blue data) and hBN (red data) are normalized to the respective Au value at contact (i.e. $h = 0$). We see that the amplitude s_3 (Fig. 3(b)) decreases within the first 50 nm above both the Au and the hBN surface, confirming the strong optical near-field confinement at the tip and that background signals are fully suppressed. Consistent with the phase images in Fig. 2(b), we find a negative phase contrast on hBN relative to the Au surface for $h = 0\,\text{nm}$ (Fig. 3(c)). Note that the retraction curves were recorded within 30 seconds, such that we can exclude interferometer drift being the cause for the smaller phase on hBN. We also find that the phase decreases when the tip is retracted above Au (blue dots), whereas it remains nearly constant when the tip is retracted above hBN (red dots). To exclude that the phase shift on Au may be caused by absorption in Au, we recorded retraction curves on Si, whose infrared absorption can be well neglected (see Supplement 1, Fig. S7). Similar to the retraction curves on Au, we observe that the phase decreases when the tip-sample distance h is increased. However, the phase shift relative to hBN and its dependence on the tip-sample distance is smaller than that observed for Au. We thus exclude that absorption in the sample causes the NPC and the decreasing phase when the tip-sample distance increases.

To better understand the s-SNOM retraction curves – and particularly the NPC – we performed calculations using the finite dipole model (FDM), which is a well-established model to quantitatively describe amplitude and phase contrasts s_n and φ_n observed in s-SNOM [31]. Indeed, Fig. 3(b,c) shows an excellent agreement between the measured (dots) and calculated (solid lines) retraction curves. In the FDM, the AFM tip is generally approximated by a prolate spheroid that is sinusoidally oscillating above the sample surface. The spheroid is characterized by its major half-axis length of $L = 300\,\text{nm}$ and an apex radius of $R = 25\,\text{nm}$. For the oscillation amplitude we specifically used $A = 50\,\text{nm}$, which is only slightly smaller than in the experiment ($A = 57\,\text{nm}$). The empirical model parameter g was set to the typically literature value, $g = 0.7e^{i0.06}$. The Au substrate and the hBN flake were modelled as semi-infinite bulk samples with a dielectric value of $\varepsilon_{\text{Au}} = -5000 + i1000$ [33] and $\varepsilon_{\text{hBN}} = 3.5$ [34], respectively. Having a closer look at the model, we find that shifts of the near-field phase φ_3 are caused by the imaginary part of the empirical
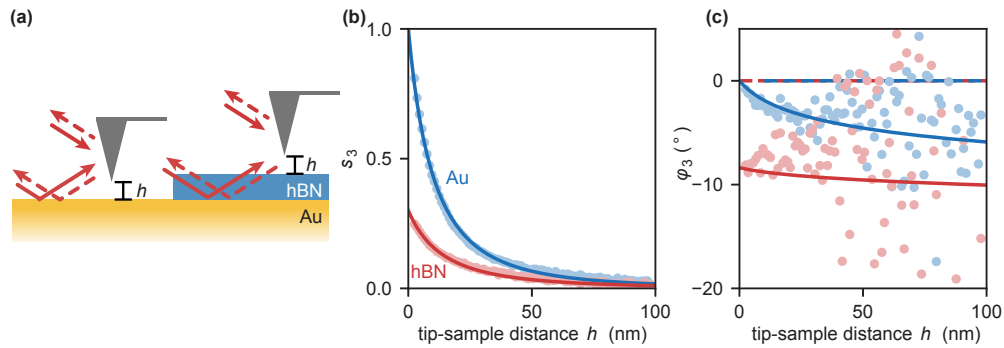
Fig. 3. Retraction curves recorded at $1000\,\mathrm{cm}^{-1}$ on a 90 nm thick hBN layer (red) and Au (blue). Tip oscillation amplitude was around 57 nm. (a) Schematics of sample and experiment. (b-c) Optical signals as a function of tip height h above the sample. (b) Amplitude s_3, (c) Phase φ_3. Dots represent experimental data, solid and dashed lines simulations within the FDM.

complex-valued factor $g = 0.7e^{i0.06}$, which was originally introduced to the model to account for radiation losses and dissipation in the tip. Indeed, repeating the calculations with a real-valued $g = 0.7$, we find on both Au and hBN the same phase $\varphi_3 = 0$, which is independent of the tip-sample distance h (horizontal blue and red dashed lines at $\varphi_3 = 0$ in Fig. 3(c), respectively). We thus attribute both the NPC and the increasing phase with decreasing tip-sample distance to larger radiative and eventually dissipative losses of the tip. More specifically, when the tip approaches a sample surface (i.e. when h decreases), the near-field interaction between tip and sample increases, which in turn increases the polarization of the tip. This increase is stronger for samples of higher reflectivity. The increasing polarization of the tip results in larger scattering (radiation losses) and dissipation within the tip, yielding an increasing positive phase shift φ_3 when the tip approaches the sample or when materials of high reflectivity are probed. As a consequence, we observe a NPC when the near-field phase of a weak dielectric material (e.g.
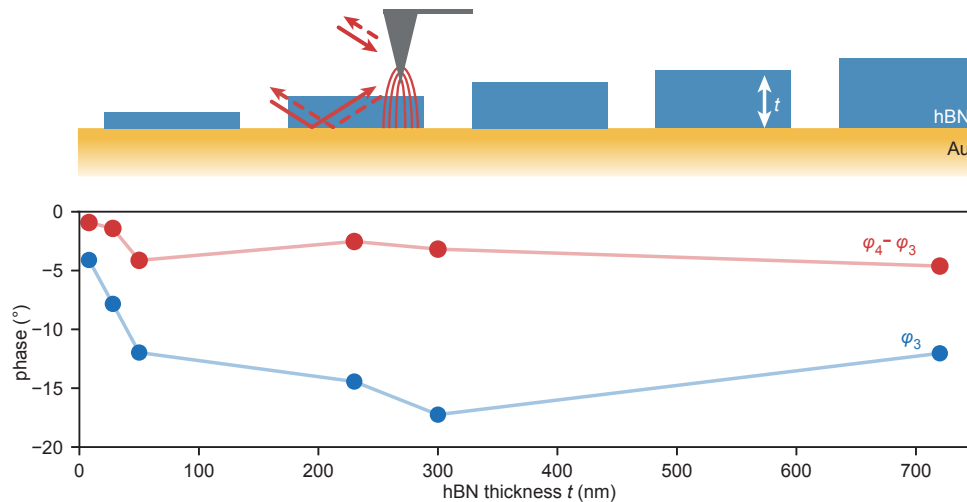

Fig. 4. Negative phase φ_3 (blue dots) and phase difference $\varphi_4 - \varphi_3$ (red dots) as a function of hBN flake thickness t. Solid lines are a guide to the eye.

hBN at $1000\,\text{cm}^{-1}$ or PMMA) is normalized to a highly reflective reference material (e.g. Au or Si), which explains the NPC observed in Figs. 1, 2.

We finally studied the phase contrast between the hBN and Au surface, φ_3, as function of the hBN thickness t (Fig. 4). For $t>90\,\text{nm}$ we find a nearly constant NPC, whereas for $t<90\,\text{nm}$ a rapid decrease of the absolute value of the NPC with decreasing hBN thickness t is observed, eventually vanishing for $t \rightarrow 0\,\text{nm}$ (blue dots in Fig. 4). The same observation is made when we plot $\varphi_4 - \varphi_3$ as a function of the hBN thickness (red dots in Fig. 4). We explain the vanishing NPC by the increasing near-field interaction between tip and Au substrate when the hBN layer becomes thinner than the near-field probing depth, which for materials with low dielectric constants such as hBN at $1000\,\text{cm}^{-1}$ is in the range of 100 nm [9]. With increasing near-field interaction between tip and Au substrate the radiative losses and dissipation by the tip increase, such that the phase contrast between thin hBN layers and the Au reference sample vanish.

4. Correction of negative phase contrasts and spectral baselines

4.1. Method A

We first discuss a typical sample where the material of interest (e.g. a weakly absorbing thin layer or a nanoscale particle) lies on top of a highly reflecting substrate (such as Si or Au), which is used to enhance s-SNOM signals [7,9,35,36] and simultaneously serves as the s-SNOM reference. As seen in Fig. 1(b,c), imaging at a single wavenumber can yield a NPC relative to the substrate in the case that the material of interest, in the following referred to as material, is non- or weakly absorbing. To clarify and quantify the absorption of the material, we suggest to construct a local phase spectrum by monochromatic imaging at various different wavenumbers, ideally including one where the material of interest is known to be non-absorbing, such that a phase baseline φ_n^b can be reliably determined. Importantly, the phase values of the material and reference need to be extracted at the same position in each image, particularly when the material thickness varies and thus changes the NPC. Subtraction of the baseline then yields a spectrum from which the correct phase (and thus absorption) contrast $\varphi_n^c(\nu) = \varphi_n(\nu) - \varphi_n^b$ can be determined for each measured wavenumber ν. We illustrate this procedure with the PMMA/PS on Si sample and data already discussed in Fig. 1. In Fig. 5(a) we show again the topography image, where we mark by blue and white dashed rectangles the areas from which the phase values for PMMA (the material of interest) and Si (the reference) were obtained by averaging. Figure 5(b) and (c) show the original (blue) and baseline-corrected (red) phase spectrum of the PMMA, respectively. The latter shows a good agreement with the nano-FTIR spectrum from which a linear baseline was subtracted (black curve, see also Supplement 1, Fig. S4).

4.2. Method B

Samples of interest may comprise various thin layers or nanoparticles of which at least one may be known to be non-absorbing in the spectral region of interest. In the case that the non-absorbing material has the same thickness and a similar refractive index as the material of interest, we suggest to use it (rather than the substrate) as a reference $\varphi_{n,\text{ref}}(\nu)$. Since the NPC between the non-absorbing reference material and the substrate can be expected to be the same as the NPC between the material of interest and the substrate, one should not observe a NPC between the material of interest and the non-absorbing reference material. We demonstrate this procedure in Fig. 5(d), showing the PMMA phase values (green dots) normalized to that of PS (reference), $\varphi_n^c(\nu) = \varphi_{n,\text{mat}}(\nu) - \varphi_{n,\text{ref}}(\nu)$, which were obtained from the areas marked in Fig. 5(a) by the blue and red rectangle, respectively. We clearly observe the PMMA peak in absence of a negative phase baseline. Note that PS in our sample has a similar thickness and has a similar refractive index as PMMA. It is also well-known to be non-absorbing in the measured spectral range, as we verify in Supplement 1, Fig. S3.
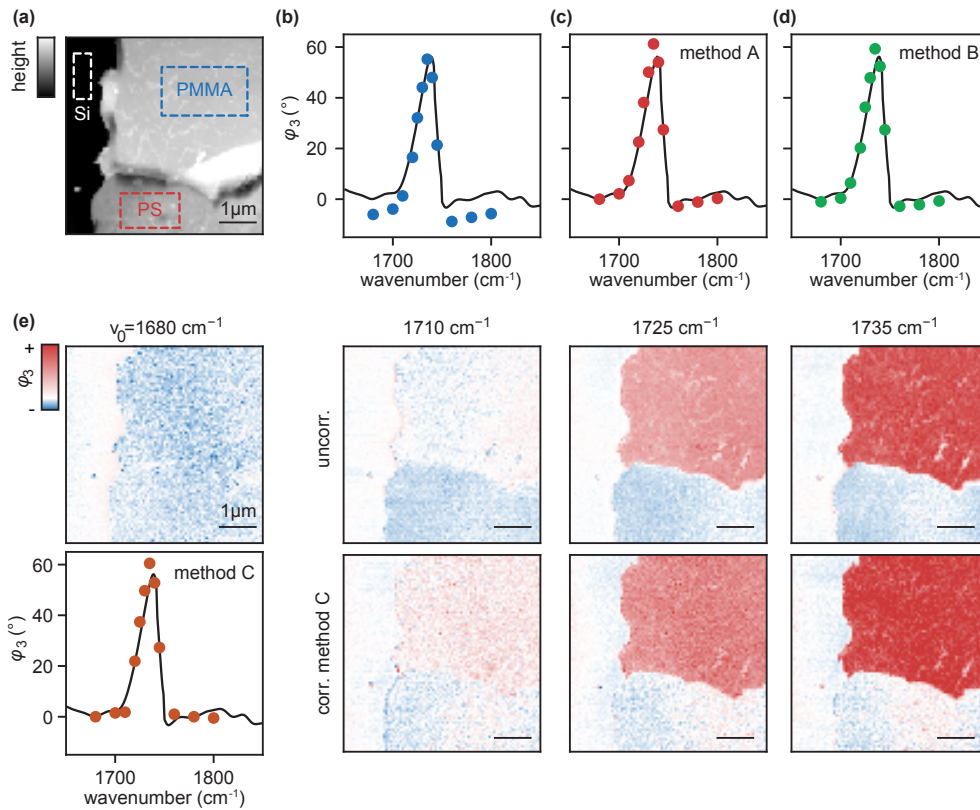
Fig. 5. Correction of the NPC. (a) Topography of the sample consisting material of interest (PMMA), PS layer and Si substrate. Marked areas indicate where the phase values have been extracted. (b) Phase spectrum constructed from the original phase images (blue dots) of the PMMA layer and baseline-corrected nano-FTIR spectrum (black curve). (c) Phase spectrum of panel (b) where a negative baseline was subtracted (red dots, method A). (d) Phase spectrum obtained by normalizing the phase values of PMMA to the phase values of PS (green dots, method B). (e) Top: original phase images at various wavenumbers normalized to the phase value of the Si substrate. Bottom: corrected phase images employing method C described in the text, together with the constructed phase spectrum (orange dots, bottom left). Negative/positive phase values are depicted in blue/red.

4.3.   Method C

We further propose a method for samples on a homogeneous reference substrate comprising materials of different sizes, shapes, and thicknesses, all of them being non-absorbing at least at one wavenumber v_0. To remove the NPC, we first take a single-wavelength image at the non-absorbing wavenumber v_0 and normalize it to the phase value of the clean substrate, yielding $\varphi_n(x, y, v_0)$. We subsequently subtract this reference image from any other phase image $\varphi_n(x, y, v_i)$ taken at wavenumbers v_i (normalized to the corresponding phase value of the substrate). We obtain NPC-corrected images $\varphi_n^c(x, y, v_i) = \varphi_n(x, y, v_i) - \varphi_n(x, y, v_0)$, from which baseline-corrected phase spectra are readily obtained by plotting the phase of the material of interest as a function of v. Importantly, prior to subtraction, careful image alignment needs to be performed, e.g., with the help of cross-correlating the topography images that are simultaneously recorded with the individual infrared images (similar to Ref. [25]). We illustrate this method again with the PMMA/PS sample on Si. In Fig. 5(e) we show various phase images (top row, uncorrected),

together with the ones where we subtracted the reference image taken at $\nu_0 = 1680\,\text{cm}^{-1}$ (bottom row). The latter ones show that the NPC between PS and Si substrate is strongly reduced. We attribute slight phase variations of about $\pm 2°$ on PS between small negative and small positive values to indirect illumination of the tip via sample reflection (similar to Fig. 2(e)). We clearly see that for the non-absorbing PS the NPC is absent for all wavenumbers. For PMMA we observe a weak positive phase contrast at $1710\,\text{cm}^{-1}$, indicating weak absorption that is not recognized in the corresponding uncorrected phase image. The PMMA phase spectrum (orange dots) extracted from the set of corrected images well reveals the PMMA peak in absence of a negative phase baseline (Fig. 5(e) bottom right). We note that the correction method proposed here could be performed online by dual-colour s-SNOM, where the reference image at ν_0 is recorded simultaneously with each image at ν_i by illuminating the tip with the corresponding two laser frequencies simultaneously (to be published elsewhere). Such simultaneous phase measurement at two frequencies could reduce the effect of drift (sample and interferometer), allowing for even more accurate mapping of very weak absorption in the sample.

5. Conclusions

We reported that a negative phase contrast (NPC) between thin films of a non-absorbing material and a highly reflective substrate (used as reference) may be observed in s-SNOM. Based on systematic experimental studies and calculations based on the empiric finite dipole model (FDM), we attribute the NPC to radiation losses (i.e. the scattering process that is the basis of s-SNOM) and eventually dissipation in the tip. For more detailed theoretical insights, full electrodynamical calculations taking into acount the entire tip geometry have to be performed in the future. Importantly, we demonstrated several simple methods for NPC correction, which rely on spectroscopic mapping (i.e. constructing a phase spectrum from a set of monochromatic s-SNOM images). They allow for separating the NPC from phase contrasts arising from infrared absorption in the sample, such that weak sample absorption can be recognized that otherwise may be masked by the NPC. Future studies could explore whether the NPC can be minimized by (i) changing the geometry or composition of the near-field probe (tip) and (ii) developing advanced imaging and correction methods (eventually by machine learning [37–40]) that can eliminate the NPC for eventually even arbitrary samples.

Supplemental document. See Supplement 1 for supporting content.

References

1. F. Keilmann and R. Hillenbrand, "Near-field microscopy by elastic light scattering from a tip," Philos. Trans. R. Soc., A **362**(1817), 787–805 (2004).
2. X. Chen, D. Hu, R. Mescall, G. You, D. Basov, Q. Dai, and M. Liu, "Modern scattering-type scanning near-field optical microscopy for advanced material research," Adv. Mater. **31**(24), 1804774 (2019).
3. N. Ocelic, A. Huber, and R. Hillenbrand, "Pseudoheterodyne detection for background-free near-field spectroscopy," Appl. Phys. Lett. **89**(10), 101124 (2006).
4. S. Amarie, T. Ganz, and F. Keilmann, "Mid-infrared near-field spectroscopy," Opt. Express **17**(24), 21794–21801 (2009).
5. F. Huth, M. Schnell, J. Wittborn, N. Ocelic, and R. Hillenbrand, "Infrared-spectroscopic nanoimaging with a thermal source," Nat. Mater. **10**(5), 352–356 (2011).
6. S. Amarie, P. Zaslansky, Y. Kajihara, E. Griesshaber, W. W. Schmahl, and F. Keilmann, "Nano-ftir chemical mapping of minerals in biological materials," Beilstein J. Nanotechnol. **3**, 312–323 (2012).

7. F. Huth, A. Govyadinov, S. Amarie, W. Nuansing, F. Keilmann, and R. Hillenbrand, "Nano-FTIR absorption spectroscopy of molecular fingerprints at 20 nm spatial resolution," Nano Lett. **12**(8), 3973–3978 (2012).

8. X. G. Xu, M. Rang, I. M. Craig, and M. B. Raschke, "Pushing the sample-size limit of infrared vibrational nanospectroscopy: from monolayer toward single molecule sensitivity," J. Phys. Chem. Lett. **3**(13), 1836–1841 (2012).

9. T. Taubner, R. Hillenbrand, and F. Keilmann, "Nanoscale polymer recognition by spectral signature in scattering infrared near-field microscopy," Appl. Phys. Lett. **85**(21), 5064–5066 (2004).

10. M. Brehm, T. Taubner, R. Hillenbrand, and F. Keilmann, "Infrared spectroscopic mapping of single nanoparticles and viruses at nanoscale resolution," Nano Lett. **6**(7), 1307–1310 (2006).

11. S. Mastel, A. A. Govyadinov, T. V. de Oliveira, I. Amenabar, and R. Hillenbrand, "Nanoscale-resolved chemical identification of thin organic films using infrared near-field spectroscopy and standard Fourier transform infrared references," Appl. Phys. Lett. **106**(2), 023113 (2015).

12. S. Berweger, D. M. Nguyen, E. A. Muller, H. A. Bechtel, T. T. Perkins, and M. B. Raschke, "Nano-chemical infrared imaging of membrane proteins in lipid bilayers," J. Am. Chem. Soc. **135**(49), 18292–18295 (2013).

13. I. Amenabar, S. Poly, W. Nuansing, E. H. Hubrich, A. A. Govyadinov, F. Huth, R. Krutokhvostov, L. Zhang, M. Knez, J. Heberle, A. M. Bittner, and R. Hillenbrand, "Structural analysis and mapping of individual protein complexes by infrared nanospectroscopy," Nat. Commun. **4**(1), 2890 (2013).

14. H. A. Bechtel, E. A. Muller, R. L. Olmon, M. C. Martin, and M. B. Raschke, "Ultrabroadband infrared nanospectroscopic imaging," Proc. Natl. Acad. Sci. **111**(20), 7191–7196 (2014).

15. B. Pollard, E. A. Muller, K. Hinrichs, and M. B. Raschke, "Vibrational nano-spectroscopic imaging correlating structure with intermolecular coupling and dynamics," Nat. Commun. **5**(1), 3587 (2014).

16. C. Westermeier, A. Cernescu, S. Amarie, C. Liewald, F. Keilmann, and B. Nickel, "Sub-micron phase coexistence in small-molecule organic thin films revealed by infrared nano-imaging," Nat. Commun. **5**(1), 4101 (2014).

17. E. A. Muller, B. Pollard, and M. B. Raschke, "Infrared chemical nano-imaging: Accessing structure, coupling, and dynamics on molecular length scales," J. Phys. Chem. Lett. **6**(7), 1275–1284 (2015).

18. C.-Y. Wu, W. J. Wolf, Y. Levartovsky, H. A. Bechtel, M. C. Martin, F. D. Toste, and E. Gross, "High-spatial-resolution mapping of catalytic reactions on single particles," Nature **541**(7638), 511–515 (2017).

19. A. de los Santos Pereira, A. Cernescu, J. Svoboda, R. Sivkova, I. Romanenko, B. Bashta, F. Keilmann, and O. Pop-Georgievski, "Conformation in ultrathin polymer brush coatings resolved by infrared nanoscopy," Anal. Chem. **92**(7), 4716–4720 (2020).

20. E. Pfitzner and J. Heberle, "Infrared scattering-type scanning near-field optical microscopy of biomembranes in water," J. Phys. Chem. Lett. **11**(19), 8183–8188 (2020).

21. C.-F. Wang, B. Kafle, T. E. Tesema, H. Kookhaee, and T. G. Habteyes, "Molecular sensitivity of near-field vibrational infrared imaging," J. Phys. Chem. C **124**(38), 21018–21026 (2020).

22. R. O. Freitas, A. Cernescu, A. Engdahl, A. Paulus, J. E. Levandoski, I. Martinsson, E. Hebisch, C. Sandt, G. K. Gouras, C. N. Prinz, T. Deierborg, F. Borondics, and O. Klementieva, "Nano-infrared imaging of primary neurons," Cells **10**(10), 2559 (2021).

23. L. Mester, A. A. Govyadinov, and R. Hillenbrand, "High-fidelity nano-FTIR spectroscopy by on-pixel normalization of signal harmonics," Nanophotonics **11**(2), 377–390 (2022).

24. T. Man, C. Xu, X.-Y. Liu, D. Li, C.-K. Tsung, H. Pei, Y. Wan, and L. Li, "Hierarchically encapsulating enzymes with multi-shelled metal-organic frameworks for tandem biocatalytic reactions," Nat. Commun. **13**(1), 305 (2022).

25. S. Paul, E. Berntsson, C. Mörman, A. Jeništová, J. Jarvet, A. Gräslund, S. Wärmländer, and A. Barth, "13c-isotope-editing of nanoscale infrared images reveals the action of an inhibitory peptide against amyloid-β aggregation," preprint (2022).

26. A. Barth, Department of Biochemistry and Biophysics, Stockhom University, Svant Arrhenius vag 16, 106 91 Stockholm, Sweden (personal communication 2022).

27. M. Johnson, Division of Surface and Corrosion Science, KHT Royal Institute of Technology, Drottning Kristinas vag 51,10044 Stockholm, Sweden (personal communication 2022).

28. A. A. Berlin, V. F. Kablov, A. A. Pimerzin, and S. S. Zlotsky, *Key Elements in Polymers for Engineers and Chemists: From Data to Applications* (CRC Press, 2014).

29. L. Mester, A. A. Govyadinov, S. Chen, M. Goikoetxea, and R. Hillenbrand, "Subsurface chemical nanoidentification by nano-ftir spectroscopy," Nat. Commun. **11**(1), 3359 (2020).

30. I. Amenabar, S. Poly, M. Goikoetxea, W. Nuansing, P. Lasch, and R. Hillenbrand, "Hyperspectral infrared nanoimaging of organic samples based on fourier transform infrared nanospectroscopy," Nat. Commun. **8**(1), 14402 (2017).

31. A. Cvitkovic, N. Ocelic, and R. Hillenbrand, "Analytical model for quantitative prediction of material contrasts in scattering-type near-field optical microscopy," Opt. Express **15**(14), 8550–8565 (2007).

32. R. Hillenbrand and F. Keilmann, "Complex optical constants on a subwavelength scale," Phys. Rev. Lett. **85**(14), 3029–3032 (2000).

33. J. Trollmann and A. Pucci, "Infrared dielectric function of gold films in relation to their morphology," J. Phys. Chem. C **118**(27), 15011–15018 (2014).

34. A. J. Giles, S. Dai, I. Vurgaftman, T. Hoffman, S. Liu, L. Lindsay, C. T. Ellis, N. Assefa, I. Chatzakis, T. L. Reinecke, J. G. Tischler, M. M. Fogler, J. H. Edgar, D. N. Basov, and J. D. Caldwell, "Ultralow-loss polaritons in isotopically pure boron nitride," Nat. Mater. **17**(2), 134–139 (2018).

35. A. Cvitkovic, N. Ocelic, J. Aizpurua, R. Guckenberger, and R. Hillenbrand, "Infrared imaging of single nanoparticles via strong field enhancement in a scanning nanogap," Phys. Rev. Lett. **97**(6), 060801 (2006).

36. M. Autore, L. Mester, M. Goikoetxea, and R. Hillenbrand, "Substrate matters: surface-polariton enhanced infrared nanospectroscopy of molecular vibrations," Nano Lett. **19**(11), 8066–8073 (2019).

37. S. Xu, A. S. McLeod, X. Chen, D. J. Rizzo, B. S. Jessen, Z. Yao, Z. Wang, Z. Sun, S. Shabani, A. N. Pasupathy, A. J. Millis, C. R. Dean, J. C. Hone, M. Liu, and D. N. Basov, "Deep learning analysis of polaritonic wave images," ACS Nano **15**(11), 18182–18191 (2021).

38. X. Chen, Z. Yao, S. Xu, A. S. McLeod, S. N. Gilbert Corder, Y. Zhao, M. Tsuneto, H. A. Bechtel, M. C. Martin, G. L. Carr, M. M. Fogler, S. G. Stanciu, D. N. Basov, and M. Liu, "Hybrid machine learning for scanning near-field optical spectroscopy," ACS Photonics **8**(10), 2987–2996 (2021).

39. X. Chen, R. Ren, and M. Liu, "Validity of machine learning in the quantitative analysis of complex scanning near-field optical microscopy signals using simulated data," Phys. Rev. Appl. **15**(1), 014001 (2021).

40. X. Chen, S. Xu, S. Shabani, Y. Zhao, M. Fu, A. J. Millis, M. M. Fogler, A. N. Pasupathy, M. Liu, and D. Basov, "Machine learning for optical scanning probe nanoscopy," arXiv preprint arXiv:2204.09820 (2022).